










## Coherent x-ray diffraction of a semiregular Pt nanodot array

Thomas F. Keller <sup>1,2,\*</sup>,† Roman Shayduk <sup>3,†</sup> Chan Kim <sup>3</sup> Nastasia Mukharamova,<sup>1</sup> Arti Dangwal Pandey <sup>1</sup>  
Manuel Abuin <sup>1</sup> Vedran Vonk <sup>1</sup> Irene Fernandez-Cuesta,<sup>2</sup> Miriam Barthelmess <sup>4</sup> Robert Frömter <sup>2,5</sup>  
Alexey Zozulya <sup>3</sup> Artur Erbe,<sup>6</sup> and Andreas Stierle<sup>1,2</sup>

<sup>1</sup>Centre for X-ray and Nano Science (CXNS), Deutsches Elektronen-Synchrotron DESY, Hamburg, Germany

<sup>2</sup>University of Hamburg, Department of Physics, Hamburg, Germany

<sup>3</sup>European XFEL GmbH, Schenefeld, Germany

<sup>4</sup>Center for Free-Electron Laser Science (CFEL), Deutsches Elektronen-Synchrotron DESY, Hamburg, Germany

<sup>5</sup>Institute of Physics, Johannes Gutenberg-Universität Mainz, Mainz, Germany

<sup>6</sup>Helmholtz Zentrum Dresden Rossendorf, Dresden, Germany



(Received 24 July 2023; accepted 21 August 2023; published 17 October 2023)

Structural insight into nano-objects down to the atomic scale is one of the most important prerequisites to understand the properties of functional materials and will ultimately permit one to relate the size and shape of nanoparticles to their catalytic activity. We elucidate the potential of extracting structural information about a small ensemble of nanoparticles that are semiregularly arranged on a periodic array from coherent x-ray Bragg diffraction. The observed fringe pattern in the Pt(111) Bragg peak obviously originates from the mutual interference of the Bragg scattered wave field from individual nanoparticles in the nanoarray. Despite the absence of a symmetry center in the Bragg peak of the nanoarray, we identify the most prominent in-plane spatial frequencies of the latter by applying a Patterson map analysis to the Bragg peak superstructure. Integration along the in-plane reciprocal space direction over the relevant in-plane regions of interest results in Laue oscillations that arise from nanoparticle sets of similar heights in real space. A one-to-one comparison with real-space microscopic information obtained from scanning electron microscopy and atomic force microscopy suggests potential nanoparticle subsets as the origin for the x-ray intensity in these regions of interest by the good agreement in their height and direction-dependent in-plane interparticle distances, as also further supported by simulations. Nanoparticle arrays with well-defined tunable sizes and lateral distances may serve in the future to track structural changes in, e.g., sizes, relative positions, and tilts of smallest catalysis-relevant nanoparticles during *operando* heterogeneous catalysis experiments in the 10-nm-size regime.

DOI: [10.1103/PhysRevB.108.134109](https://doi.org/10.1103/PhysRevB.108.134109)

### I. INTRODUCTION

X-ray diffraction can provide three-dimensional (3D) information on nanostructures down to the atomic scale [1–3]. The high penetration depth of x rays facilitates experiments in harsh environments such as liquids or gases, and hence they are an ideal probe for dynamically tracking nanoparticles *in situ* or *operando* [4,5].

To study heterogeneous catalysis, x rays can be utilized to probe nanoparticle ensembles and track their reaction-induced size and shape changes during oxidation [1,6] or sintering [7] down to the single nanoparticle level [8]. In the latter case, isolated nanostructures such as single nanoparticles with long-range crystalline order over the x-ray coherence length are rocked through a Bragg reflection in the x-ray beam and a stack of reciprocal space detector images is collected. Phase retrieval algorithms permit one to deduce the crystalline electron density and strain state in real space from the reconstructed amplitude and phase of the diffracted wave field.

This so-called coherent x-ray diffraction imaging (CXDI) has matured over the last two decades and was used to analyze single nanoparticles *ex situ* [9,10]. More recently, the tracking of dynamic changes under various *in situ* conditions has been reported, elucidating the temporal evolution of strain and defects in single nanoparticles [8,11,12]. For single alloy nanoparticles with often superior properties, e.g., bimetallic PtRh, the shape and compositional strain profile were followed while changing the gas environment from oxidizing to reducing [13], and from inert to catalytic reaction conditions [14].

To gain more insight into the role of mutual nanoparticle interactions and the nanoparticle support, it is desirable to analyze nanostructure arrangements consisting of more than a single nanoparticle, but far less than the large ensembles investigated so far. Periodic nanostructures can be characterized in terms of the superlattice period, composition profile, and lattice mismatch of the crystalline features by analyzing the interference of coherently diffracted x rays [15–17]. One reported example deals with lithographically produced, periodically arranged Cu<sub>3</sub>Au nanocuboids prepared from an epitaxially grown film, which are coherently illuminated by the x-ray beam. The resulting x-ray interference pattern

\*thomas.keller@desy.de

†T. F. Keller and R. Shayduk equally contributed to this work.

indicated that the nanocuboids exhibited a decreased order-disorder transition temperature during annealing as compared to a closed thin film, stressing the role of the long-range order in such 2D binary alloy systems [18]. Moreover, intensity modulations in surface x-ray diffraction patterns arising from a superlattice interference provide information on the registry and distance of nanoclusters as small as 1.5 nm in diameter that are arranged on superlattice sites [19,20]. Calculations showed that the diffraction pattern from a two-dimensional quantum dot (QD) array can be inverted to obtain the correct QD shape and orientation [21,22]. In imperfect nanoarray samples, however, the analysis of the coherent x-ray Bragg diffraction signal is often restricted to the superlattice interferences, as small imperfections obstruct a phase retrieval and, in turn, the real-space reconstruction by CXDI. Imperfections with less long-range order may originate from (i) a non-negligible size distribution of the nano-objects, (ii) spread in their crystal orientation and tilt, and (iii) in their relative mutual positions. This represents the general situation of a small nanoparticle ensemble. In grazing incidence small-angle x-ray scattering (GISAXS) geometry, being insensitive to the exact atomic positions, the average shape of the QD islands was reconstructed by an iterative phase retrieval algorithm [23]. Similarly, the small-angle forward-scattering rather than the Bragg diffraction signal was utilized for CXDI in transmission geometry to successfully reconstruct the real-space electron density distribution of a set of multiple Au nanocrystals arranged in close vicinity [24]. Although the reconstruction is easier and more reliable in GISAXS or transmission geometry, Bragg-based CXDI can provide more structural details including the strain state, defects [12], and even the location of charge density wave domains in high-temperature superconductors [25].

Here, we analyze the coherent x-ray diffraction pattern of a semiregular array of platinum (Pt) nanodots created by electron beam lithography (EBL) on a (100)-oriented strontium titanate (STO) single crystal supported by simulations. EBL permits one to create small nanoparticle ensembles or periodic nanodot arrays with a narrow size distribution and tune their size and interparticle distance. The Pt nanodot arrangement was too complex for a reconstruction by the currently available phase retrieval algorithms. We therefore exploited a windowed fast Fourier transform (FFT) to extract structural information from regions of interest within the 3D coherent x-ray diffraction pattern, similar to applying the Patterson function to single crystal data [26]. We show that it is possible to connect in-plane spatial frequencies of the nanodot array deduced from the Patterson plot and out-of-plane thickness oscillations to identify nanoparticle sets in the complementary real-space scanning electron (SEM) and atomic force (AFM) microscopic images. Based on real- and reciprocal-space correlations, we suggest how this approach of extracting structural information from coherent scattering patterns of such nanostructure arrangements can be generalized. We discuss prerequisites to deduce nanoparticle sizes and interparticle distances, allowing for *in situ* tracking of dynamic processes under operating conditions. The flexible design of EBL-prepared nanoparticle ensembles combined with different algorithms in the analysis of coherent diffraction data from a small number of nanoparticles opens diverse

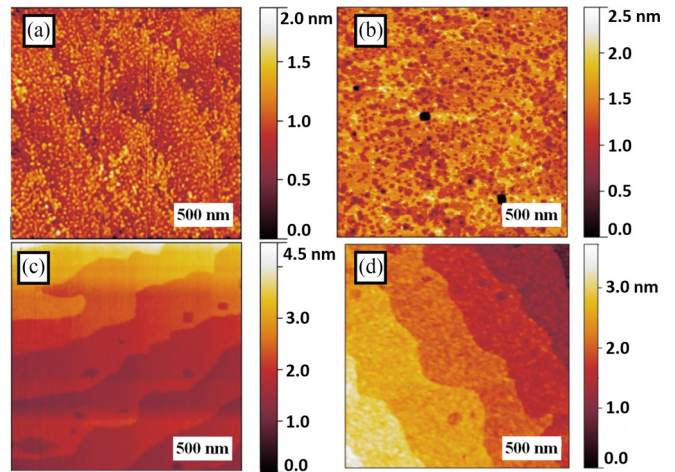


FIG. 1. AFM surface topography of subsequent surface preparation steps to introduce a single  $\text{TiO}_2$ -terminated surface functionality on the epi-polished, (100)-oriented, STO single crystal. (a) As received; (b) after a 30 sec dip into BOE; (c) after subsequent annealing at  $950^\circ\text{C}$  in air for 1 hour exhibiting atomic steps with  $\text{TiO}_2$  termination according to [30]; and (d) after deposition of an 8-nm-thick Pt film. The lateral image size is  $2 \times 2 \mu\text{m}$  and the corresponding height information is given in the scale bars on the right.

approaches to elucidate processes in various scientific disciplines, which are not yet sufficiently understood. In catalysis, these include, e.g., the size-dependent strong metal-support interaction (SMSI) [27,28] and adjacent nanoparticle-induced nanoparticle size, shape, and strain state changes.

## II. MATERIALS AND METHODS

### A. Materials

Epi-polished, 0.5 wt.%, Nb doped, (100)-oriented STO crystals with a specified miscut angle of  $< 0.1^\circ$  and an (010) edge orientation were used as substrates. All chemicals were used as delivered without further purification.

### B. Preparation and characterization of the STO crystal substrate surface

To induce a  $\text{TiO}_2$  termination [29] as a single surface functionality on the (100)-oriented STO crystals, we modified a protocol of Koster *et al.* [30]. In short, the as-received STO crystals were ultrasonically soaked in ultrapure water for 10 min, subsequently dipped for 30 sec into a diluted hydrofluoric acid solution (buffered oxide etch, BOE), rinsed twice in ultrapure water, and dried in a  $\text{N}_2$  stream. Afterwards, the STO crystals were annealed in a tube furnace in air by ramping up the temperature at a rate of 20 K/min up to  $950^\circ\text{C}$ , holding for 1 h, and leaving to cool down to room temperature. Subsequently, a homogeneous, 8-nm-thick Pt layer was deposited onto the annealed STO crystal at room temperature with an electron beam evaporator (deposition rate 0.02 nm/sec, pressure  $7 \times 10^{-7}$  mbar, sample rotation 10 rpm, purity of Pt 99.99%).

Figure 1 shows topographic AFM images of the STO crystal surface during these different steps of the surface pretreatment. The heterogeneous surface morphology of the

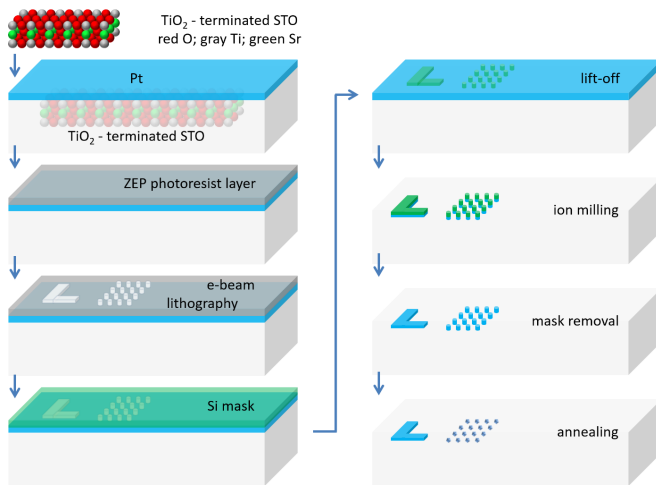


FIG. 2. Sketch of the sequential steps to create STO-supported Pt nanodot arrays (not to scale) by electron-beam lithography, and a combined lift-off and etching, followed by annealing, modified from Ref. [32].

as-received STO(100) single crystal in Fig. 1(a) turns into irregularly arranged plateau areas of discrete height levels, as shown in Fig. 1(b), after ultrasonic bathing in deionized water, 30 sec dip in BOE, cleaning twice in deionized water, and drying in a stream of nitrogen. After annealing at 950 °C in air for 1 hour, the crystal steps in Fig. 1(c) with a terrace width of about 200 nm formed in agreement with a crystal surface miscut of around  $0.1^\circ$ . Depositing an 8-nm-thick Pt film leads to a fine roughening visible in Fig. 1(d), while the surface steps remain apparent. A three-layer fit to model the x-ray reflectivity (XRR) indicates a total Pt film thickness of 8.7 nm with a surface roughness of 0.63 nm, whereas the STO/Pt interfacial roughness is only 0.28 nm; see, e.g., Fig. S1 in the Supplemental Material [31].

### C. Electron beam lithography to create Pt nanodot arrays

To create Pt nanodot arrays, we modified a protocol of Komanicky *et al.* [32] as sketched in Fig. 2. A 275-nm-thick ZEP photoresist layer was spin coated onto the Pt film on top of the STO crystal, after the latter was precleaned in acetone and isopropanol for 15 min followed by drying in a stream of  $N_2$ . Prebake and postbake were done on a hotplate for 10 min at  $T = 180^\circ\text{C}$ . Square nanodot arrays with mutual center-center interdot distances of 70–200 nm between adjacent nanodots, and varying dose rates to create different Pt nanodot sizes of around 30–60 nm, were created in the photoresist by electron beam lithography using 20 kV, a magnification of 2000 $\times$ , a beam current of 0.23 nA, and a working distance of 9.6 mm without applying a proximity correction [33]. The nanodot arrays were surrounded by hierarchically arranged marker structures serving as guidance to simplify the relocalization of preselected regions of interest at the x-ray beam line. The nanodot array discussed in the following was created using a nominal nanodot diameter of 50 nm and a center-center distance of 150 nm.

The resist was developed for 90 sec in n-amylacetate, rinsed with isopropanol, and dried in a stream of  $N_2$ . Sub-

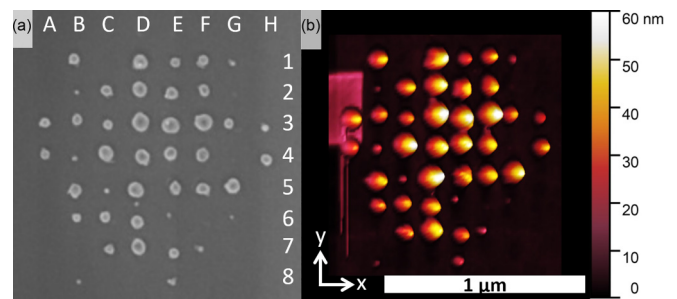


FIG. 3. (a) SEM and (b) AFM height image in 3D view of the Pt nanodot array. Characters A–H on the top and numbers 1–8 on the right in (a) designate the individual nanodots. The white arrows in (b) indicate the directions of the spatial coordinates, and the color bar on the right corresponds to height levels from 0 to 60 nm.

sequently, the electron-beam structured surface was covered with a 100-nm-thick Si mask by evaporating Si from a granulate inside a Knudsen cell under UHV, heated to nominally 1450 °C at a pressure of less than  $2 \times 10^{-9}$  mbar over the deposition time of 10 hours. Afterwards, the crystal was immersed into dimethyl sulfoxide (DMSO), cleaned in acetone, and subsequently ultrasonicated for 5 min in DMSO to facilitate the lift-off, followed by rinsing in acetone and isopropanol and drying in a stream of  $N_2$ . Pt in the unprotected area was selectively removed by an  $Ar^+$  ion etching for 60 sec using a Kaufman ion source (base pressure  $2.4 \times 10^{-6}$  mbar,  $Ar^+$  ion beam current 15 mA, beam voltage 500 V, discharge voltage 38 V, acceleration voltage 125 V, Ar flux 2 ml/min, process pressure  $2.5 \times 10^{-4}$  mbar). The electrical conductivity of a similarly thick Pt film on a sapphire crystal mounted aside was used as a reference to determine the time, after which the uncapped Pt film was etched away to stop the etching process. Electrical contacts to the reference sample were established by ultrasonic wedge bonding. Then, the remaining Si mask material was removed by immersing the sample into NaOH at 80 °C for 1 h. Finally, the Pt nanodot-array sample was heated up in a tube furnace in air at a moderate temperature of 750 °C, compromising a nonequilibrium shape of the Pt nanodots and avoiding their dewetting and disappearance. For the annealing, a heating rate of 20 °C/min was used and the sample was kept at the annealing temperature for 10 min. Subsequently, the tube furnace was let to cool down.

### D. SEM and AFM characterization

Figures 3(a) and 3(b) show SEM and AFM height images of the Pt nanodot array.

The SEM image was obtained with a high-resolution field-emission microscope [34] operated at 2 kV using a through-lens detector in secondary electron imaging mode. The AFM topographic image was collected in tapping mode in air [34] with a standard tapping mode silicon cantilever (cantilever frequency 300 kHz, cantilever stiffness 40 N/m, scan rate 2 Hz). A second-order plane fit was applied and the terraces were aligned with a three-point leveling function to correct for the bending movement of the piezoelectric crystal. While the lateral diameter  $d$  of each nanodot was determined



TABLE I. Height  $h$  and lateral diameter  $d$  of the Pt nanoparticles within the  $8 \times 8$  nanodot array as determined from AFM and SEM image analysis, respectively.

	A	B	C	D	E	F	G	H
1 $h$ (nm)		51.4		56.5	32.6	43.2	21.7	
$d$ (nm)		44.3		62.8	40.6	44.5	21.0	
2 $h$ (nm)		14.9	49.8	50.1	43.5	43.0		
$d$ (nm)		18.4	45.3	70.0	57.5	44.5		
3 $h$ (nm)	48.9	43.9	40.8	60.0	59.3	60.5	45.0	31.3
$d$ (nm)	41.5	43.2	36.2	77.2	71.9	76.1	40.5	24.2
4 $h$ (nm)	37.7	25.8	64.4	53.0	55.9	47.5		49.0
$d$ (nm)	40.1	19.6	73.0	64.1	53.6	58.8		40.6
5 $h$ (nm)		52.6	20.4	58.6	45.1	50.1	59.8	
$d$ (nm)		54.7	17.1	69.3	51.0	48.4	61.5	
6 $h$ (nm)		44.3	47.2	46.3	16.0		10.7	
$d$ (nm)		34.0	43.1	56.2	15.5		13.0	
7 $h$ (nm)			43.5	55.0	45.0	23.4		
$d$ (nm)			34.0	64.1	41.8	23.0		
8 $h$ (nm)		22.2			29.0			
$d$ (nm)		15.5			24.8			

by image analysis from the SEM image, the height  $h$  was obtained from the corrected AFM topography image.

Table I lists the individual height and lateral diameter for each of the nanodots in the array. The mean nanodot height was deduced to be  $h = 42.8 \pm 14$  nm. We assign the overall decreasing dot size and increasing number of missing nanodots towards the out-of-center regions of the array pattern to the proximity effect, giving rise to over-illumination during the electron-beam lithographic process in the central part [33]. In turn, this leads to an insufficient dose in noncentral regions and explains the heterogeneity and related comparatively large standard deviation in the mean nanodot size. A slight rectangular elevation visible on the left side of the AFM in Fig. 3(b) is due to a thin carbon contamination layer around two nanodots arising from high-magnification SEM imaging after the x-ray experiment.

### E. Coherent x-ray Bragg diffraction

The coherent x-ray Bragg diffraction experiment was conducted in the experimental hutch 2 of the coherence applications beam line P10 at the synchrotron PETRA III at DESY in Hamburg, Germany. The x-ray beam was focused by compound refractive lenses (CRLs) to a beam size of  $3 \times 2 \mu\text{m}$  in the horizontal and vertical direction, respectively, resulting in a footprint of around  $12 \times 2 \mu\text{m}$  on the STO crystal surface. A sketch of the scattering geometry is shown in Fig. 4. The sample-to-detector distance was 5 m. The degree of coherence inside the focus was around 30% in the horizontal direction, while it was of the order of 70% in the vertical direction [35,36]. The x-ray Bragg diffraction signals of the Pt(111) Bragg peak showing coherent interference fringes were collected on a 2D silicon pixel detector with  $487 \times 619$  pixels, each sized  $172 \times 172 \mu\text{m}$ . The x-ray energy that was used was 13 keV, corresponding to a wavelength  $\lambda = 0.095$  nm. The STO crystal was vertically mounted onto a piezo stage, aligned to the x-ray beam

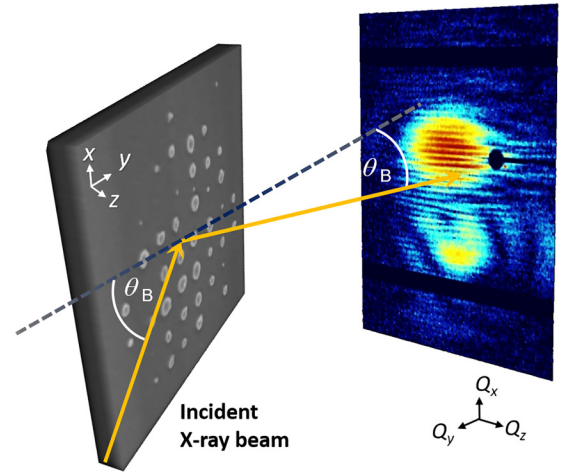


FIG. 4. Sketch of the experimental setup for the coherent x-ray Bragg diffraction experiment. Arrows indicate the coordinate directions in the sample frame in real and reciprocal space.

and rocked through an angular range of  $0.7^\circ$  around the incident Bragg angle of  $\theta_B = 12.4^\circ$  to probe the reciprocal space around the Pt(111) Bragg peak at  $2\theta = 24.8^\circ$ . Several nanodot arrays on the STO crystal were imaged by SEM [34] and subsequently preselected by saving the position coordinates of the nanodot arrays and the hierarchically arranged Pt marker structures. Figures 5(a) and 5(b) show a sketch of the marker design used for the EBL process and an SEM image of the resulting large marker that was around  $100 \mu\text{m}$ .

After the transfer to the x-ray beam line, an optical microscope was used for a coarse sample alignment. To relocalize a preselected Pt nanodot array on the STO surface, the sample was scanned by a lateral translation through the x-ray beam. A nanotransfer protocol was utilized to find (i) the sample edges, (ii) the hierarchically arranged Pt markers written by electron-beam lithography, and (iii) the preselected nanodot arrays.

The guiding markers were detected by the characteristic Pt x-ray fluorescence using a Si drift energy-dispersive x-ray fluorescence detector mounted along the surface normal with an energy resolution of 140 eV full width at half maximum (FWHM). An energy window was set around the  $\text{Pt}_{L\alpha 1}$  edge at 9.36 keV; see, e.g., the overview and high-resolution x-ray scanning images in Figs. 5(c) and 5(d), and the correspondence between the SEM overview and the Pt x-ray fluorescence scanning image in Fig. S2 in the Supplemental Material [31]. A slightly longer elongation of the marker signal in Fig. 5(d) along the horizontal as compared to the vertical direction reflects the shape of the x-ray footprint on the sample surface.

Coherent x-ray Bragg diffraction signals of the nanodot array were collected by rocking the sample over an angular range of  $0.7^\circ$  while collecting a detector image for each of the 61 steps. From the set of 61 detector images, a three-dimensional coherent x-ray Bragg diffraction signal was reconstructed as follows. The reciprocal-space coordinates  $Q_x$ ,  $Q_y$ ,  $Q_z$  of the scattering vector  $Q$  in the sample frame, as defined in Fig. 4, were calculated and assigned for each pixel of the detector image for all 61 rocking angles.

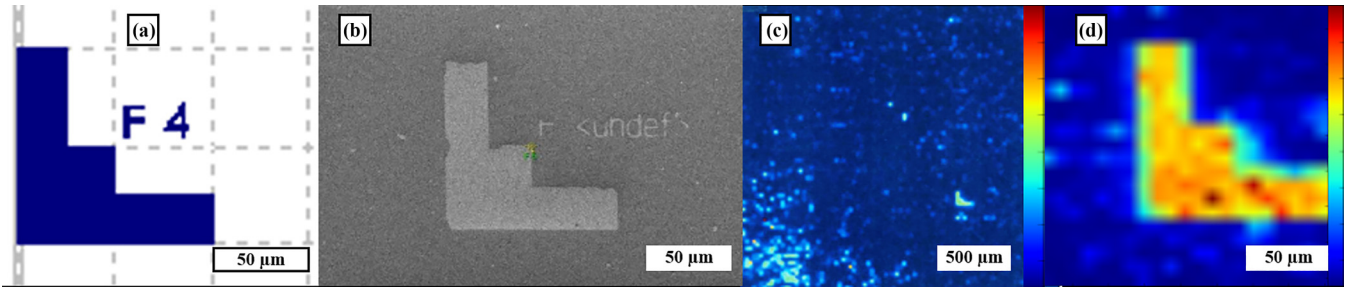


FIG. 5. (a) Sketch of a marker written into the photoresist by electron-beam lithography used to relocate the nanodot array. (b) SEM image of a resulting Pt marker. (c) Overview Pt x-ray fluorescence scanning image indicating the coarse marker position. (d) High-resolution x-ray fluorescence scanning image to achieve a precise relocation of the preselected nanodot array.

The 3D reciprocal scattering data were linearly interpolated to form a 3D scalar field defined on an evenly spaced 3D grid in reciprocal space (see, e.g., a 2D raw detector image in Fig. S3, and an image sequence of the scan through the Pt(111) Bragg peak to obtain the full 3D reciprocal scattering data in the movie M1 in the Supplemental Material [31]). The zero is shifted to the position of the ideal Pt(111) reciprocal lattice point determined from the Pt lattice constant 0.3924 nm at 293.15 K [37].

### F. Simulation of coherent x-ray Bragg diffraction intensity distribution

To simulate the in-plane coherent scattering intensity distribution, we employed the program PYNX [38]. Individual substrate-supported nanodots were permitted to vary in their relative positions  $x$  and  $y$ , their radius  $r$ , and their azimuthal and normal lattice tilt with respect to the crystal orientation of the substrate. Each nanodot was described as a half sphere and accordingly filled with Pt atoms regularly arranged on Pt FCC crystal lattice sites  $n_i$  with orthogonal dimensions  $n_x = 400$ ,  $n_y = 400$ ,  $n_z = 400$ , such that each site was filled inside the half sphere of the nanodot. The lattice parameter of Pt was chosen from the literature [37]. Each Pt atom was assumed to coherently scatter the incident x rays, and the far-field diffraction intensity to arise as overlay from mutual interferences of x rays scattered from any of the Pt atoms. The influence of nanoparticle size, strain, and tilt on the resulting diffraction pattern was systematically simulated for selected regions of interest in reciprocal space. Nanoparticle tilts were simulated by rotating the crystal lattice sites of one or more selected nanoparticles by a given azimuthal or out-of-plane angle. Elastic strain was added by simultaneously expanding the lattice uniformly along all orthogonal directions using the direction-independent strain  $\epsilon$ , e.g.,  $x_{\text{strained}} = (1 + \epsilon)x_0$ ,  $y_{\text{strained}} = (1 + \epsilon)y_0$ , and  $z_{\text{strained}} = (1 + \epsilon)z_0$ , where the index 0 indicates the unstrained state.

## III. RESULTS AND DISCUSSION

The ensemble of, in total, 42 nanodots arranged on the  $8 \times 8$  array as is seen in the SEM and AFM images in Fig. 3 was analyzed by coherent x-ray Bragg diffraction using the scattering geometry sketched in Fig. 4.

Figure 6(a) shows a three-dimensional plot of the iso-intensity surface obtained from the 3D scattering data. The

interference fringes observed around the Pt(111) Bragg peak indicate a preferential Pt(111)/STO(100) orientation of coherently scattering nano-objects with finite size. Figure 6(b) displays a section of three orthogonal slices through the 3D scattering data. The protruding rodlike structure in Fig. 6(a) is the so-called crystal truncation rod signal arising from the STO substrate surface. The discontinuous intensity distribution along the crystal truncation rod in Fig. 6(a) is arising from the discrete sampling.

In the following, we describe how structural information can be extracted from the 3D x-ray intensity in Fig. 6. We discuss to which extent characteristic distances present in the Bragg peak superstructure can be correlated to the real-space SEM and AFM images of the original nanoarray in Fig. 3. For this purpose, we divide the discussion into first the out-of-plane direction normal to the substrate surface, and then the in-plane direction.

*Out-of-plane direction.* From the periods of oscillations along  $Q_z$  of the 3D intensity distribution in reciprocal space in Fig. 6(a), essentially three characteristic oscillation periods can be identified. For a more detailed analysis of the nanoparticle height information along  $Q_z$ , it is instructive to look into a central and otherwise arbitrary  $Q_z = \text{const}$  slice, as shown in Fig. 7(a) for  $Q_z$  equal to  $0.15 \text{ nm}^{-1}$ . Despite the rich in-plane interference fringes from the nanodot array in

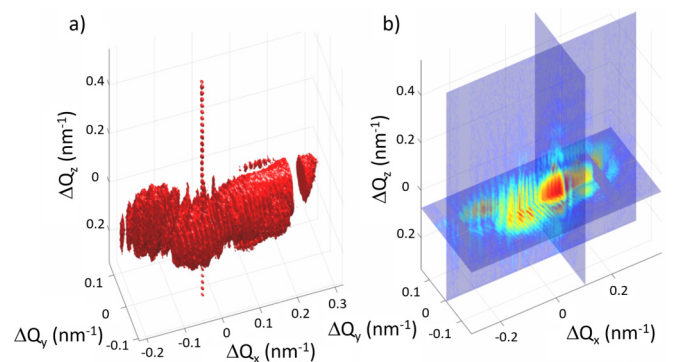


FIG. 6. (a) 3D intensity distribution in reciprocal space from the Pt nanodot array assembled from the stack of 2D detector images taken at different tilt angles  $\theta$ . A  $|Q| = \text{const}$  iso-intensity surface was drawn at an arbitrarily chosen value of 16 counts. (b) Three orthogonal slices through the 3D scattering data. The color code corresponds to the logarithm of the number of counts at a given point in reciprocal space.

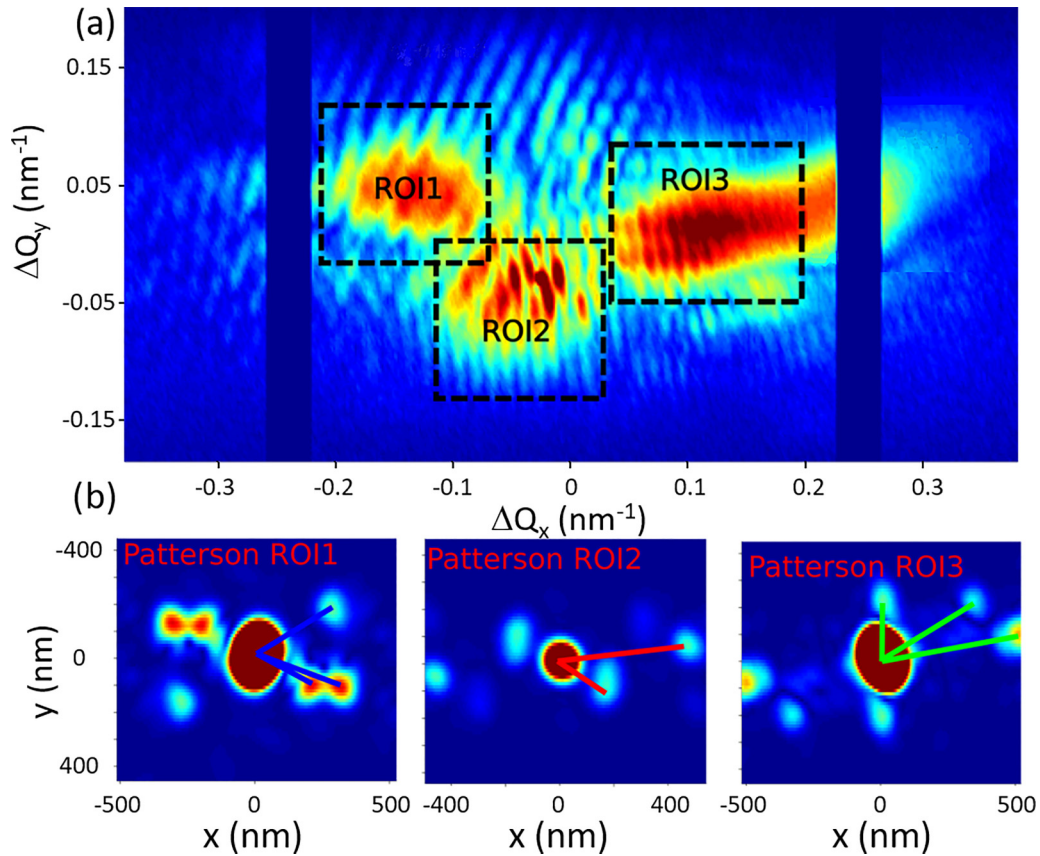


FIG. 7. (a)  $Q_z = 0.15 \text{ nm}^{-1}$  slice showing the intensity distribution in the  $Q_x$  and  $Q_y$  directions. Dashed rectangles indicate three regions of interest (ROI) that were analyzed separately. (b) Patterson maps obtained by applying the windowed FFT to the  $Q_z$ -slice data for each of the ROI1–ROI3. Blue, red, and green lines indicate dominant interparticle correlation lengths and orientations for each ROI.

the  $Q_x$ - $Q_y$  plane evident from Fig. 7(a), quantitative height information of the nanoparticles contributing to the diffraction signal can be extracted from the out-of-plane direction. To constrain and categorize the experimental data set and to simplify the discussion of the out-of-plane direction, we select three in-plane regions of interest, as indicated by the dashed frames in Fig. 7(a). For each of the three framed ROIs, we integrate the in-plane signal for each  $Q_z$  point of the grid. The results of the analysis are shown in Fig. 8.

The color-map graphs in Fig. 8 show the intermediate data after the  $Q_x$  integration, whereas the linear plots are obtained by the full in-plane  $Q_x$ - $Q_y$  integration of the respective ROIs. We assign the characteristic oscillations along the  $Q_z$  direction in the linear plots in Fig. 8 to finite-particle-height Laue oscillations originating from the x-ray interference at the nanodot array. Accordingly, the height  $h$  of the nanoparticle arrangement giving rise to the scattering signal is related to the mean width of a single oscillation  $\Delta Q_z$  as  $\Delta Q_z = 2\pi/h$ .

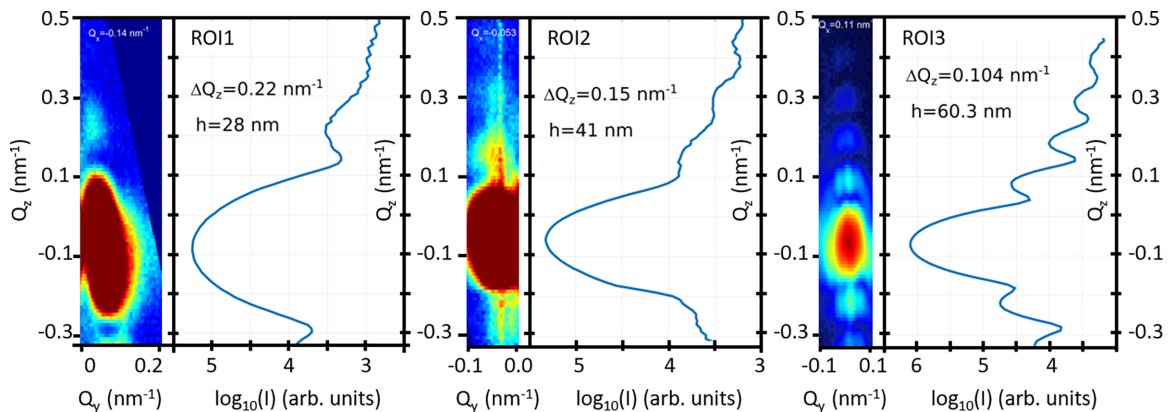


FIG. 8.  $Q_y$ - $Q_z$  maps and  $Q_z$  plots of 1D and 2D integrations, respectively, of the three regions of interest shown in Fig. 7(a).



We deduce for ROI1 a height  $h$  of the nano-objects of 28 nm. Similarly, the ROI2 signal is created from objects of 41 nm in height, while the ROI3 signals stem from around 60 nm high objects. Note the good agreement between these nanoparticle height values as extracted from the selected ROIs in Fig. 7(a) and the AFM results listed in Table I, indicating that height values of individual nanoparticles are lying between 20 and 65 nm if one neglects the very few outliers mainly located on the nanodot-array border.

*In-plane direction.* As the incident x-ray beam is only partially transverse coherent, each Bragg-diffracting nanoparticle should be understood as a partially coherent light source. For the chosen diffraction geometry, the transverse beam coherence mostly plays a role. The intensity at a given point in the detector plane, therefore, consists of coherent and incoherent contributions, where  $Q$  is the scattering vector,

$$I(Q) = \alpha I_{\text{incoh}}(Q) + \beta I_{\text{coh}}(Q). \quad (1)$$

The incoherent part does not form particle-particle interference fringes and is simply equal to the incoherent sum of intensities from individual nanoparticles (NPs) NP $_j$ :

$$I_{\text{incoh}}(Q) = \sum_j I_{\text{NP}_j}(Q). \quad (2)$$

On the other hand, the coherent contribution to the intensity,

$$I_{\text{coh}}(Q) \propto \left[ \sum_j F_{\text{NP}_j}(Q) \right] \left[ \sum_j F_{\text{NP}_j}(Q) \right], \quad (3)$$

does form mutual interference fringes [39].

As introduced above, Fig. 7(a) is the  $Q_z = 0.15 \text{ nm}^{-1}$  slice through the 3D scattering data. Since the lateral dimension of the larger single nanoparticles,  $d$ , is of the order of 60 nm (see, e.g., Table I), the corresponding reciprocal space shape function is around  $0.1\text{--}0.2 \text{ nm}^{-1}$  FWHM, provided the nanoparticle is fully crystalline. This size is roughly equal to the apparent size of each of the three intensity maxima marked as ROI1–ROI3 in Fig. 7(a), and we therefore assign the structural features within these ROIs to Bragg peaks of individual nanoparticles. This fractionation in the  $Q_x$ – $Q_y$  plane indicates relative mutual tilts of the crystal lattices that translate to around  $0.4^\circ$ ,  $0.7^\circ$ , and  $1.0^\circ$  between ROI1 and ROI2, ROI2 and ROI3, and ROI1 and ROI3, respectively. The diffraction signal of nanoparticles can only contribute to a ROI if their relative particle tilt angle  $\alpha$  fulfills the condition

$$\tan \alpha = dQ_{x,y} \ll \lambda/d. \quad (4)$$

For the x-ray wavelength  $\lambda = 0.095 \text{ nm}$  and a nanoparticle diameter of  $d \approx 60 \text{ nm}$ , a maximum angle of  $\approx 0.09^\circ$  can be deduced. For larger tilts of the nanoparticles, such as for those observed for ROI1–ROI3 with  $\alpha \geq 0.4^\circ$ , their shape functions are completely separated in reciprocal space and the interference fringes of the diffraction pattern cannot be analyzed as a whole or be assigned to a single set of coherently scattering nanoparticles.

To relate the interference fringes with an approximate size of  $\Delta Q_{x,y} = 0.01\text{--}0.02 \text{ nm}^{-1}$  to the original real-space structure of the nanodot array, we exploit a windowed FFT. Similar to the Patterson function for a crystal lattice, the windowed

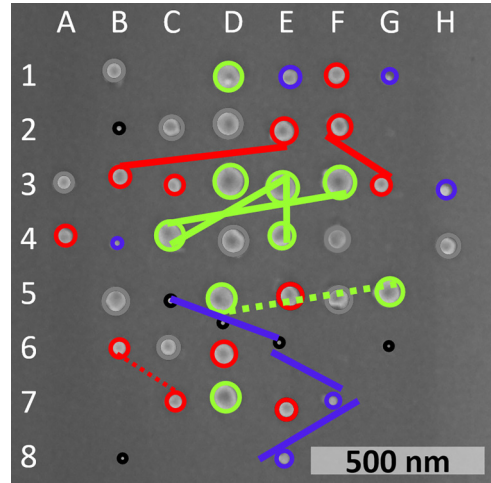


FIG. 9. Lateral interparticle correlation lengths and orientations from the Patterson maps to scale in the SEM image of the nanodot array. The color of the lines indicates the Laue height for each associated ROI. Nanoparticles are encircled in colors to classify their heights in ranges of 65–55 nm (green), 54–47 nm (gray), 46–36 nm (red), and 33–23 nm (blue), and below 22 nm (black).

FFT provides information on interparticle vectors. Figure 7(b) shows three windowed FFTs obtained from each of the ROIs utilizing a Gaussian window in the reciprocal space map in Fig. 7(a). Around eight different particle-particle distances can be observed, as indicated by the colored lines in Fig. 7(b). To identify candidate nanoparticles within the nanodot array, we translated the colored lines from the windowed FFTs into the SEM image in Fig. 9, keeping to scale the exact lengths and directions of all eight particle-particle position correlations.

Moreover, the nanoparticles in Fig. 9 are encircled with a color code indicating height levels obtained from AFM (see, e.g., Table I), while the color of the lines reflects the height obtained from the out-of-plane direction for a given ROI. For each ROI, the color lines were arranged such that they are connecting nanoparticles of height levels obtained from the Laue analysis satisfying both the in-plane and out-of-plane constraints at the same time. We implicitly assume here that all nanoparticles contributing to the scattering signal inside the ROI have the same height level, which is reasonable in view of the rather sharp Laue fringes along  $Q_z$  in Fig. 8. This, on the other hand, also means that the nanoparticle sets within the ROIs exhibit a similar height and relative tilts below  $0.09^\circ$ . A potential nanoparticle subset giving rise to the scattering intensity in ROI3 with a nanoparticle height of  $\sim 60 \text{ nm}$  as deduced by the Laue analysis can be identified in the center of the nanodot array. All three full green lines are connecting close-by nanoparticles that are matching the height range 55–65 nm. The dashed green line indicates an alternative nanoparticle pair that similarly fulfills the constraints in their heights and mutual lateral arrangement imposed by the Patterson and Laue analyses. For ROI2, the full red lines similarly connect two candidate nanoparticle sets with a size of 43.9 and 43.5 nm for the first two and 43.0 and 45.0 nm for the second set, in close agreement with the Laue result of around 41 nm. For the shorter correlation length that resembles the

diagonal of the nanodot-array lattice, two alternative subsets are marked with red dotted lines in the lower part with similar nanoparticle height values of 44.3 and 43.5 nm, and 46.3 and 45.0 nm.

For the nanoparticle sets with the smallest heights of around 28 nm in ROI1, a simultaneous attribution of nanoparticles, in agreement with both the Patterson and Laue results, is not straightforward. Apart from the limited number of nanoparticles in that size regime, the smallness of the ROI1 nanoparticles implies a broader reciprocal-space signal and related less-precise size information. An assignment can accordingly be made if one permits a larger deviation in the in-plane lengths and directions from the real nanoparticle positions as well as in the heights levels as compared to ROI2 and ROI3. Following this line of argument, the blue lines in Fig. 9 are connecting, in total, four nanoparticles from the blue and black size range with a mean height level of 22 nm.

Overall, combining the Patterson and Laue analyses with the AFM and SEM imaging suggests potential nanoparticle candidates for each of the selected ROIs from which the scattering signal could originate. It should, however, be noted that the selection of the nanoparticle sets is not unique and does not generally permit a one-to-one correspondence of single nano-objects, as is also indicated by the dashed lines in Fig. 9, suggesting alternative assignment options. We still argue that for this particular nanodot array, several independently coherent scattering, i.e., aligned subgroups, of nano-objects, can be identified by their convincing correspondence in the windowed FFTs and the SEM, as well as in the Laue and AFM height values. This assignment largely relies on the existence of nanoparticle tilts, which are splitting up the Bragg peak of the nanodot array such that each part has sufficient angular separation from the particle subsets, permitting one to restrict the analysis to localized ROIs in reciprocal space.

*Simulation of coherent scattering intensity distribution.* The relevance of crystal tilting for the nanodot array analyzed here is further elucidated by simulations, which are required as today's existing phase retrieval algorithms are not capable of reconstructing the experimentally obtained intensity distribution. To better understand the origin of the latter, we simulated the coherent scattering intensity of a selected nanoparticle subset in reciprocal space and analyzed the influence of the nanoparticle size, relative in-plane arrangement in  $x$  and  $y$ , tilt, and strain. For simplicity, we chose the intensity distribution in the  $Q_x$ - $Q_y$  plane in ROI2 in Fig. 7(a). The Patterson map in Fig. 7(b) suggests that it predominantly originates from three individual nanodots of the Pt nanodot array, with angular directions and relative lateral distances as indicated by the red lines. In Fig. 9, these lines interconnect nanodots belonging to the height category "red," identifying a similar height within 46–36 nm as suggested by the Laue oscillations of ROI2 along  $Q_z$  in Fig. 8. The simulated diffraction patterns discussed in the following are calculated by considering that x rays are coherently scattered by the three-nanoparticle subset using the PYNX code [38]. The origin of the interference fringes within ROI2 was systematically elucidated by purposely introducing a crystal tilt for nanoparticle 3, inducing an angular isolation of the scattering pattern in reciprocal space, as discussed in the section above. The isolation is clearly visible in Fig. S4(b) in the Supplemental Material [31], where the intensity spot at

around  $Q_x = 0.25 \text{ nm}^{-1}$  is predominated by circular interference fringes originating from the  $0.15^\circ$ -tilted nanoparticle 3. In contrast, the diffraction signals from nanoparticles 1 and 2 in Fig. S4(b) are overlapping and coherently interfere, creating fringes directed normal to the mean direction in the Patterson map, e.g., along the yellow arrow in Fig. S4(a) (see Supplemental Material [31]). Figure S4 further elucidates how the simulated intensity distribution in ROI2 depends on the diameters of the nanoparticles for selected sizes: Figs. S4(b)–S4(d):  $d_{\text{NP1}} = d_{\text{NP2}} = d_{\text{NP3}} = 34.0 \text{ nm}$ ; Figs. S4(f)–S4(h):  $d_{\text{NP1}} = 44.5 \text{ nm}$ ,  $d_{\text{NP2}} = 40.5 \text{ nm}$ ,  $d_{\text{NP3}} = 34.0 \text{ nm}$ ; and Figs. S4(j)–S4(l):  $d_{\text{NP1}} = 44.5 \text{ nm}$ ,  $d_{\text{NP2}} = 40.5 \text{ nm}$ ,  $d_{\text{NP3}} = 60.0 \text{ nm}$ , and selected uniform strain states, with  $\epsilon$  as defined in Sec. II F, i.e., Figs. S4(b), S4(f), S4(j):  $\epsilon = 0.00$ ; Figs. S4(c), S4(g), S4(k):  $\epsilon = 0.03$ ; Figs. S4(d), S4(h), S4(l):  $\epsilon = 0.15$ . Equivalently, Fig. S5 in the Supplemental Material [31] shows the intensity distribution of the two-nanoparticle interference fringes in ROI2 for the other two nanoparticle pairs, NP1-NP3 and NP2-NP3; see the yellow arrows in Figs. S5(a) and S5(e), where the tilt of NP2 and NP1 was set to  $0.15^\circ$ , respectively. Here, nanoparticle diameters were chosen as  $d_{\text{NP1}} = 43.2 \text{ nm}$ ,  $d_{\text{NP2}} = 57.5 \text{ nm}$ ,  $d_{\text{NP3}} = 34.0 \text{ nm}$  and the strained state was simulated as in Fig. S4 to vary as follows: Figs. S4(b), S4(f):  $\epsilon = 0.00$ ; Figs. S4(c), S4(g):  $\epsilon = 0.03$ ; and Figs. S4(d), S4(h):  $\epsilon = 0.15$ . Figures S4 and S5 overall elucidate the origin of the interference fringes as coherent superpositions of a small number of scattering nanoparticles and stress the sensitivity to strain in clearly visible intensity levels and shifts of the fringe position in reciprocal space. The simulation results in Fig. 10 furthermore suggest that the experimentally determined intensity in ROI2 reflects a slight crystal tilt of NP3 of  $= 0.025^\circ$ , while the tilts of NP1 and NP2 are zero, when comparing the all-aligned and tilted nanoparticle scenario in Figs. 10(a) and 10(b), respectively. For each, the top images are the intensity distributions in the whole simulated reciprocal-space region, whereas the bottom shows magnifications from the central region that corresponds to ROI2 in Figs. 7(a) and 10(f). Comparing Figs. 10(b)–10(d) for  $\epsilon = 0.000$ ,  $\epsilon = 0.003$ ,  $\epsilon = 0.030$ , respectively, with Fig. 10(f) indicates that although there is strain sensitivity (see the systematic variation in strain levels in Fig. S6 in the Supplemental Material [31]), a dominating influence of strain in the three-nanoparticle subset is not present.

#### IV. CONCLUSION

We analyzed the coherent x-ray diffraction pattern of an ensemble of more than 40 nanoparticles and identified several nanoparticle subsets as potential candidates that dominate the reciprocal-space intensity in selected regions of interest. Correlative microscopy based on Pt markers close to the nanodot array permitted one to combine in-plane and out-of-plane x-ray scattering data in reciprocal space with real-space scanning-force and electron microscopy. We supported the nanoparticle assignment by simulating the coherent diffraction from three-nanoparticle subsets with angular directions and distances taken from the applied Patterson analysis. The simulated interference patterns show overall good agreement with the experimental x-ray intensity in view of the spatial frequencies inside the analyzed regions of interest



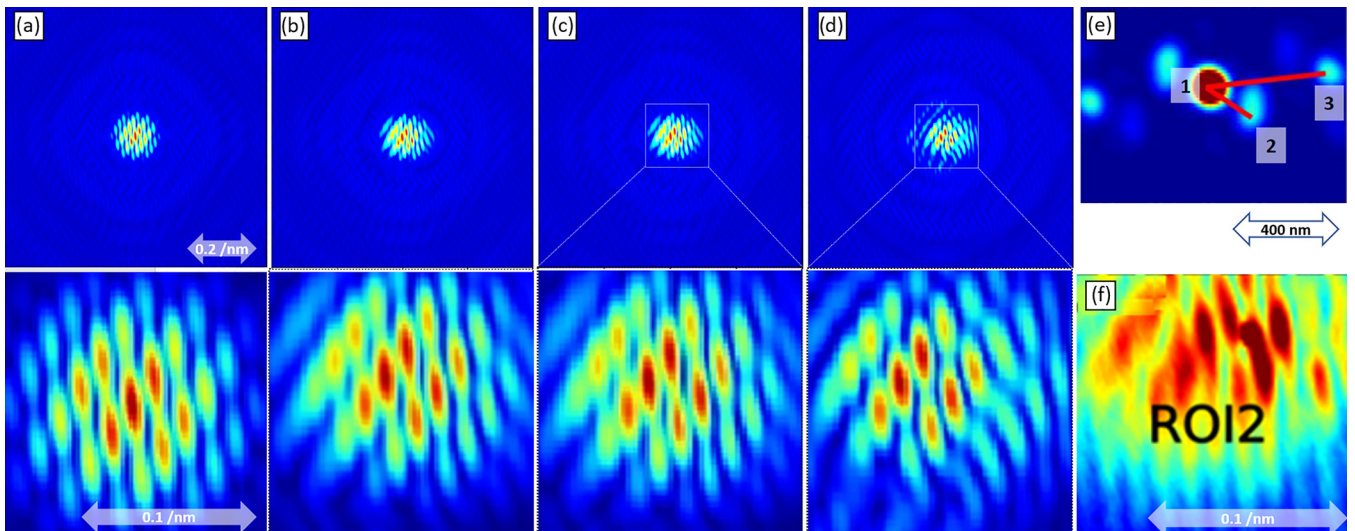


FIG. 10. (a)–(d) Simulation of the coherent Bragg diffraction intensity in ROI2 assuming a three-nanoparticle subset with different crystal tilts and strain. Nanoparticle diameters are  $d_{\text{NP1}} = 43.2$  nm,  $d_{\text{NP2}} = 57.5$  nm, and  $d_{\text{NP3}} = 34.0$  nm, resembling nanoparticles B3, E2, and B6 or C7, respectively. Top: simulated intensity; bottom: magnification of the central region. (a)  $\epsilon = 0.000$ , tilts of nanodots 1–3 = 0; (b)–(d) tilts of nanodots 1 and 2 = 0, tilt of nanodot 3 =  $0.025^\circ$ ; (b)  $\epsilon = 0.000$ , (c)  $\epsilon = 0.003$ , (d)  $\epsilon = 0.030$ . (e) Simulated Patterson map with main angular directions and distances [see, e.g., Fig. 7(b)], indicating the main contributions in real space. (f) Experimental intensity in the  $Q_x$ - $Q_y$  plane in ROI2. More details of the simulated three-nanodot arrangements are given in the main text.

and indicate that nanoparticle tilts are important to consider besides nanoparticle strain. For the particular nanodot array discussed here, the interference between particles in the in-plane direction has enhanced the visibility of the height fringes in the  $z$  direction of a nanoparticle subset with similar height and tilt and facilitates the corresponding data treatment.

In the future, the data analysis could be refined by further restricting the ROIs in the coherent x-ray maps to selected minima and maxima of the  $Q_x$ - $Q_y$  fringes and deduce the corresponding height by integrating  $Q_z$  from that particular region. The analysis of such coherent diffraction patterns may be simplified by adjusting those geometric parameters of the nanoarrays that can easily be controlled during the EBL process, e.g., introducing a larger interparticle spacing and reducing the nanoparticle size, giving more direct evidence of the origin of interference fringes. Also, the structural refinement could be further detailed by a multi-Bragg peak analysis, providing additional constraints on the origin of the scattered x-ray intensity in the real-space nanoarray.

Overall, in this work, we could elucidate how coherent x-ray Bragg diffraction can be utilized to extract structural details of less-perfect but rather common nanoparticle assem-

blies without the need to rely on phase retrieval algorithms with a limited capability of handling structurally rich arrangements. Such an approach can allow one to potentially track nanoparticle size and shape changes under *in situ* or *operando* reaction conditions, providing valuable insight into reaction-induced sintering processes.

## ACKNOWLEDGMENTS

We acknowledge the access granted to the coherence beam line P10 at PETRA III at DESY and the excellent support by the beam-line staff and the beamline manager Michael Sprung. This project has received funding from the European Union's Horizon 2020 research and innovation programme under Grant Agreement No. 101007417, Nanoscience Foundries and Fine Analysis (NFFA) Europe-Pilot.

We thank Claudia Neisser and Jochen Kerbusch from the Helmholtz Zentrum Dresden Rossendorf, Dresden, Germany, for the EBL processing, and Carsten Thönißen and Alexander Neumann, University of Hamburg, Department of Physics, Hamburg, Germany, for the assistance with the ion etching.

- [1] P. Nolte, A. Stierle, N. Kasper, N. Y. Jin-Phillipp, N. Jeutter, and H. Dosch, Reversible shape changes of Pd nanoparticles on MgO(100), *Nano Lett.* **11**, 4697 (2011).  
 [2] C. Giannini, M. Ladisa, D. Altamura, D. Siliqi, T. Sibillano, and L. De Caro, X-ray diffraction: A powerful technique for the multiple-length-scale structural analysis of nanomaterials, *Crystals* **6**, 87 (2016).

- [3] F. Meirer and B. M. Weckhuysen, Spatial and temporal exploration of heterogeneous catalysts with synchrotron radiation, *Nat. Rev. Mater.* **3**, 324 (2018).  
 [4] R. Westerström, J. Gustafson, A. Resta, A. Mikkelsen, J. N. Andersen, E. Lundgren, N. Seriani, F. Mittendorfer, M. Schmid, J. Klikovits, P. Varga, M. D. Ackermann, J. W. Frenken, N. Kasper, and A. Stierle, Oxidation of Pd(553): From ultrahigh

- vacuum to atmospheric pressure, *Phys. Rev. B* **76**, 155410 (2007).
- [5] A. Stierle and E. Vlieg, Surface-sensitive x-ray diffraction methods, in *Modern Diffraction Methods*, edited by E. J. Mittemeijer and U. Welzel (Wiley-VCH, Weinheim, Germany, 2012), pp. 221–257.
- [6] P. Müller, U. Hejral, U. Rütt, and A. Stierle, *In situ* oxidation study of Pd-Rh nanoparticles on MgAl<sub>2</sub>O<sub>4</sub> (001), *Phys. Chem. Chem. Phys.* **16**, 13866 (2014).
- [7] U. Hejral, P. Müller, O. Balmes, D. Pontoni, and A. Stierle, Tracking the shape-dependent sintering of platinum-rhodium model catalysts under *operando* conditions, *Nat. Commun.* **7**, 10964 (2016).
- [8] M. Abuin, Y. Y. Kim, H. Runge, S. Kulkarni, S. Maier, D. Dzhigaev, S. Lazarev, L. Gelisio, C. Seitz, M. I. Richard, T. Zhou, V. Vonk, T. F. Keller, I. A. Vartanyants, and A. Stierle, Coherent x-ray imaging of CO-adsorption-induced structural changes in Pt nanoparticles: Implications for catalysis, *ACS Appl. Nano Mater.* **2**, 4818 (2019).
- [9] M. A. Pfeifer, G. J. Williams, I. A. Vartanyants, R. Harder, and I. K. Robinson, Three-dimensional mapping of a deformation field inside a nanocrystal, *Nature (London)* **442**, 63 (2006).
- [10] D. Dzhigaev, T. Stankevič, Z. Bi, S. Lazarev, M. Rose, A. Shabalin, J. Reinhardt, A. Mikkelsen, L. Samuelson, G. Falkenberg, R. Feidenhans’L, and I. A. Vartanyants, X-ray Bragg ptychography on a single InGaN/GaN core-shell nanowire, *ACS Nano* **11**, 6605 (2017).
- [11] D. Kim, M. Chung, S. Kim, K. Yun, W. Cha, R. Harder, and H. Kim, Defect dynamics at a single Pt nanoparticle during catalytic oxidation, *Nano Lett.* **19**, 5044 (2019).
- [12] J. Carnis, A. R. Kshirsagar, L. Wu, M. Dupraz, S. Labat, M. Texier, L. Favre, L. Gao, F. E. Oropeza, N. Gazit, E. Almog, A. Campos, J. S. Micha, E. J. Hensen, S. J. Leake, T. U. Schüllli, E. Rabkin, O. Thomas, R. Poloni, J. P. Hofmann *et al.*, Twin boundary migration in an individual platinum nanocrystal during catalytic CO oxidation, *Nat. Commun.* **12**, 5385 (2021).
- [13] T. Kawaguchi, T. F. Keller, H. Runge, L. Gelisio, C. Seitz, Y. Y. Kim, E. R. Maxey, W. Cha, A. Ulvestad, S. O. Hruszkewycz, R. Harder, I. A. Vartanyants, A. Stierle, and H. You, Gas-induced segregation in Pt-Rh alloy nanoparticles observed by *in situ* Bragg coherent diffraction imaging, *Phys. Rev. Lett.* **123**, 246001 (2019).
- [14] Y. Y. Kim, T. F. Keller, T. J. Goncalves, M. Abuin, H. Runge, L. Gelisio, J. Carnis, V. Vonk, P. N. Plessow, I. A. Vartanyants, and A. Stierle, Single alloy nanoparticle x-ray imaging during a catalytic reaction, *Sci. Adv.* **7**, eabh0757 (2021).
- [15] W. J. Bartels, *Characterization of Superlattices by X-Ray Diffraction* (Springer, Boston, MA, 1987), pp. 441–458.
- [16] M. Sugawara, M. Kondo, S. Yamazaki, and K. Nakajima, Exact determination of superlattice structure by small-angle x-ray diffraction, *J. Cryst. Growth* **93**, 318 (1988).
- [17] L. Sorba, G. Bratina, A. Franciosi, L. Tapfer, G. Scamarcio, V. Spagnolo, A. Migliori, P. Merli, and E. Molinari, Si-GaAs(001) superlattice structure, *J. Cryst. Growth* **127**, 121 (1993).
- [18] T. Schüllli, J. Trenkler, I. Mönch, D. Le Bolloc’h, and H. Dosch, X-ray study of the structure and order in lithographic Cu<sub>3</sub>Au nano-cuboids, *Europhys. Lett.* **58**, 737 (2002).
- [19] D. Franz, S. Runte, C. Busse, S. Schumacher, T. Gerber, T. Michely, M. Mantilla, V. Kilic, J. Zegenhagen, and A. Stierle, Atomic structure and crystalline order of graphene-supported Ir nanoparticle lattices, *Phys. Rev. Lett.* **110**, 065503 (2013).
- [20] D. Franz, N. Blanc, J. Coraux, G. Renaud, S. Runte, T. Gerber, C. Busse, T. Michely, P. J. Feibelman, U. Hejral, and A. Stierle, Atomic structure of Pt nanoclusters supported by graphene/Ir(111) and reversible transformation under CO exposure, *Phys. Rev. B* **93**, 045426 (2016).
- [21] I. A. Vartanyants and I. K. Robinson, Imaging of quantum array structures with coherent and partially coherent diffraction, *J. Synchrotron Radiat.* **10**, 409 (2003).
- [22] M. Dupraz, S. J. Leake, and M. I. Richard, Bragg coherent imaging of nanoprecipitates: Role of superstructure reflections, *J. Appl. Crystallogr.* **53**, 1353 (2020).
- [23] I. A. Vartanyants, I. K. Robinson, J. D. Onken, M. A. Pfeifer, G. J. Williams, F. Pfeiffer, H. Metzger, Z. Zhong, and G. Bauer, Coherent x-ray diffraction from quantum dots, *Phys. Rev. B* **71**, 245302 (2005).
- [24] Y. Kim, J. Kim, K. W. Ahn, D. Y. Noh, C. Kim, H. C. Kang, H. C. Lee, and C. J. Yu, Quantitative coherent x-ray diffraction imaging of multiple nanoparticles, *J. Korean Phys. Soc.* **70**, 849 (2017).
- [25] I. Robinson, T. A. Assefa, Y. Cao, G. Gu, R. Harder, E. Maxey, and M. P. Dean, Domain texture of the orthorhombic phase of La<sub>2-x</sub>Ba<sub>x</sub>CuO<sub>4</sub>, *J. Supercond. Novel Magn.* **33**, 99 (2020).
- [26] A. L. Patterson, A fourier series method for the determination of the components of interatomic distances in crystals, *Phys. Rev.* **46**, 372 (1934).
- [27] L. Liu and A. Corma, Metal catalysts for heterogeneous catalysis: From single atoms to nanoclusters and nanoparticles, *Chem. Rev.* **118**, 4981 (2018).
- [28] Y. Li, Y. Zhang, K. Qian, and W. Huang, Metal-support interactions in metal/oxide catalysts and oxide-metal interactions in oxide/metal inverse catalysts, *ACS Catal.* **12**, 1268 (2022).
- [29] V. Vonk, S. Konings, G. J. Van Hummel, S. Harkema, and H. Graafma, The atomic surface structure of SrTiO<sub>3</sub>(0 0 1) in air studied with synchrotron x rays, *Surf. Sci.* **595**, 183 (2005).
- [30] G. Koster, B. L. Kropman, G. J. Rijnders, D. H. Blank, and H. Rogalla, Quasi-ideal strontium titanate crystal surfaces through formation of strontium hydroxide, *Appl. Phys. Lett.* **73**, 2920 (1998).
- [31] See the Supplemental Material at <http://link.aps.org/supplemental/10.1103/PhysRevB.108.134109> for the x-ray reflectivity data to determine the original platinum layer thickness, scanning electron and x-ray scanning overview images used for the localization and correlation of the region of interest, a 2D raw detector image (sequence), and simulations of the systematic dependence on nanoparticle sizes and strain.
- [32] V. Komanicky, H. Lddir, K. C. Chang, A. Menzel, G. Karapetrov, D. Hennessy, P. Zapol, and H. You, Shape-dependent activity of platinum array catalyst, *J. Am. Chem. Soc.* **131**, 5732 (2009).
- [33] E. Soe, B. K. Choi, and O. Kim, Determination of proximity effect parameters and the shape bias parameter in electron beam lithography, *Microelectron. Eng.* **53**, 305 (2000).
- [34] A. Stierle, T. F. Keller, H. Noei, V. Vonk, and R. Roehlsberger, DESY NanoLab, *JLSRF* **2**, A76 (2016).
- [35] A. V. Zozulya, S. Bondarenko, A. Schavkan, F. Westermeier, G. Grübel, and M. Sprung, Microfocusing transfocator for 1D

- and 2D compound refractive lenses, *Opt. Express* **20**, 18967 (2012).
- [36] A. Singer and I. A. Vartanyants, Coherence properties of focused X-ray beams at high-brilliance synchrotron sources, *J. Synchrotron Radiat.* **21**, 5 (2014).
- [37] J. W. Arblaster, Crystallographic properties of platinum, *Platinum Metal. Rev.* **50**, 118 (2006).
- [38] V. Favre-Nicolin, G. Girard, S. Leake, J. Carnis, Y. Chushkin, J. Kieffer, P. Paleo, and M. I. Richard, PyNX: High-performance computing toolkit for coherent x-ray imaging based on operators, *J. Appl. Crystallogr.* **53**, 1404 (2020).
- [39] K. Bagschik, J. Wagner, R. Buß, M. Riepp, A. Philippikobs, L. Müller, J. Buck, F. Trinter, F. Scholz, J. Seltmann, M. Hoesch, J. Viehhaus, G. Grübel, H. P. Oepen, and R. Frömter, Direct 2D spatial-coherence determination using the Fourier-analysis method: Multi-parameter characterization of the P04 beamline at PETRA III, *Opt. Express* **28**, 7282 (2020).